Bestelldatum: 2009-30-10 07:16:39
Bestellnummer: SUBITO-2009103000097

UBA
Universitätsbibliothek Augsburg

Universitätsbibliothek Augsburg D-86135 Augsburg

Yerevan State University library

Alex Manoogyan 1
375049 Yerevan
AM

Subito-Bestellung
normal

Tel-Nr. +374 1 551334
E-mail: elpub@ysu.am
Fax:
u 8 Subito Library International

Die Auslieferung sollte spätestens erfolgen bis: **04.11.2009 07:20**

Angaben zum bestellten Dokument:

Lieferart: **EMAIL**
Lieferform: COPY PDF

Signatur:	**85 85/UA 4210.1**
Titel Zeitschrift / Werk:	**Japanese journal of applied physics / 1**
Band / Heft:	**44 / 10**
Ersch.-Jahr:	**,2005**
Seiten:	**7494-7499**
Aufsatztitel:	
Autor (Artikel):	**Feng W. et al**
Autor / Hrsg. (Werk):	
Ort / Verlag:	**: Tokyo,Oyo Butsuri Gakkai**
ISSN / ISBN:	**0021-4922**
Kundenspezifische Infos:	,
Kontaktperson/Bemerkung:	Ms Izabela Ohanyan

Bitte beachten Sie:

Sie erhalten die Rechnung für diese Lieferung über die Subito-Zentralregulierung.
REKLAMATIONEN bitte unbedingt innerhalb von 10 Tagen an die Lieferbibliothek senden.

Wir weisen den Empfänger darauf hin, dass Sie nach geltendem Urheberrecht die von uns übersandten Vervielfältigungsstücke ausschließlich zu Ihrem privatem oder sonstigen eigenen Gebrauch verwenden und weder entgeltlich noch unentgeltlich in Papierform oder elektronische Kopie verbreiten dürfen.

Universitätsbibliothek Augsburg
Dokumentenlieferung subito
Universitätsstr.22
D-86159 Augsburg

Kontakt:
Gabriele Kellner
Tel.: ++49-821-598-5386
Fax.: ++49-821-577-020
e-mail: subito@bibliothek.uni-augsburg.de

Japanese Journal of Applied Physics
Vol. 44, No. 10, 2005, pp. 7494–7499

©2005 The Japan Society of Applied Physics

Ultrasonic-Assisted Synthesis of Poly(3-hexylthiophene)/TiO_2 Nanocomposite and Its Photovoltaic Characteristics

Wei FENG*, Yiyu FENG and Zigang WU

Department of Polymer Materials Science and Engineering, School of Materials Science and Engineering, Tianjin University, Tianjin 300072, China

(Received February 17, 2005; revised June 15, 2005; accepted June 17, 2005; published October 11, 2005)

The nanocomposites of poly(3-hexylthiophene) (PAT6) encapsulating titanium oxide (TiO_2) with different TiO_2 weight fractions were synthesized by *in situ* ultrasonic-assisted polymerization, and investigated in terms of their optical properties, microstructures and photoconductivity. The interaction between PAT6 and TiO_2 and the nature of chain growth were investigated and explained according to the results of Fourier transform infrared spectroscopy (FTIR). The increase in conjugation length of the polymer and the improvement of crystallinity with an increase in TiO_2 weight fraction were investigated and explained according to the results of UV–vis absorption spectroscopy, photoluminescence spectroscopy and X-ray diffractometry (XRD). Particle dimensions were measured and the nature of association between the components was observed by scanning electron microscopy (SEM) and transmission electron microscopy (TEM) techniques. The photoconductivity of the PAT6/TiO_2 composite increased markedly and was discussed by taking the photoinduced charge transfer between PAT6 and TiO_2 into consideration. [DOI: 10.1143/JJAP.44.7494]

KEYWORDS: conducting polymer composites, poly(3-hexylthiophene), titanium oxide (TiO_2), nanocomposites, photoconductivity

1. Introduction

Polymer-based photovoltaics is a growing area of research that holds promise for the creation of low-cost flexible devices for commercial applications. In particular, conjugated polymer-based solar cells could offer many advantages in terms of fabrication, such as low-cost roll-to-roll production of large-area flexible solar cells. Because of these advantages, the development of polymer solar cells is expected to have a major impact.[1,2] However, the poor photoinduced charge separation and transport of photogenerated charges in many conjugated polymers are considered responsible for the low efficiencies of their energy conversion.[3]

The discovery of photoinduced electron transfer in the composites of conducting polymers as donors and organic molecules as acceptors has provided a molecular approach to highly efficient photovoltaic conversion.[4–6] Achieving an efficient donor–acceptor cell relies upon the optimization of underlying processes: (1) photon absorption, (2) exciton diffusion, (3) photoinduced electron transfer at the donor-acceptor interface, and (4) an effective migration of charged species to their respective electrodes.

The formation of conjugated polymer–inorganic nanocomposites is considered a promising approach to an effective incorporation of titanium oxide into devices with possible synergetic effects.[7,8] Organic/inorganic nanocomposites are very promising for applications in devices such as light-emitting diodes, photodiodes, photovoltaic cells, and gas sensors.[9] Since the properties of a nanocomposite film can be easily changed by varying its composition, such materials are highly versatile, while their fabrication shares the same advantages as those of conventional organic device technology, such as low-cost production and the possibility of device fabrication on large areas and flexible substrates. The applications of different organic–inorganic nanocomposites to organic solar cells[10–13] have been reported.

The performance of polymer–inorganic nanoparticle bulk heterojunction solar cells will be strongly dependent on the charge transport properties of the composite as well as its morphology, which will determine exciton dissociation efficiency.[14,15] Usually, in a dispersed heterojunction device, both the photocurrent generation and charge transport are functions of morphology. Photocurrent generation requires a uniform blending on the scale of exciton diffusion length, while charge transport requires continuous paths from interfaces to contacts. Methods for further improvement of donor–acceptor device performance involve increasing the charge transport capability of component materials, understanding and controlling the nanoscale morphology of the film, and broadening the spectral response of active materials. However, the conjugated polymer–inorganic nanocomposites showed inhomogenities associated with nanoparticle agglomeration; therefore, it was difficult to determine precisely how the nanoparticle affected the conjugated polymer and the device properties.

Titanium oxide is a well-known photoactive catalytic system, and has a large surface area with a spongelike structure and consistent characteristics over a wide range of temperatures. The use of a polymer–TiO_2 cell increases the overall device efficiency by increasing surface area and interpenetration between the electron accepting TiO_2 and the adsorbed sensitizing donor molecule.[16] Currently, there are many approaches to the creation of a polymer–TiO_2 photovoltaic device. Polythiophene is more attractive for nanocrystalline TiO_2 photovoltaic devices due to its environmental stability, hole mobilities of higher than 0.1 $cm^2\ V^{-1}\ S^{-1}$ and tailorable chemical properties.[17,18]

In order to improve the application of PAT6/TiO_2 nanocomposites in photovoltaic devices, it has been of considerable interest to study the interactions between PAT6 and TiO_2 nanoparticles, which can result in realizing the novel optic–electronic properties of PAT/TiO_2 composites. Generally, it has been thought that TiO_2 nanoparticles can act as charge carriers, or electro-optically active centers that influence the optical and electronic properties of PAT6.[19] The interfacial structure effects between PAT6 and TiO_2 have only been investigated recently. However, they are still

*Corresponding author. E-mail address: lf@xjtu.edu.cn

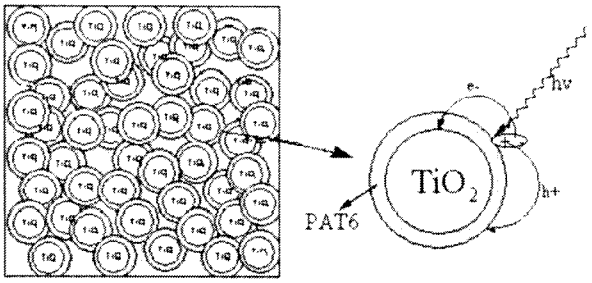

Fig. 1. Scheme of photoinduced charge transfer between poly(3-hexylthiophene) and TiO_2.

largely unknown in this research field. In this study, a nanocomposite of poly(3-hexylthiophene) (PAT6) encapsulating titanium oxide with different TiO_2 weight fractions was synthesized by in situ polymerization, and the interface structural effects between PAT6 and TiO_2 nanoparticles were investigated by UV–vis, PL spectroscopy, scanning electron microscopy (SEM), transmission electron microscopy (TEM), Fourier transform infrared spectroscopy (FTIR) and X-ray diffractometry (XRD). The photoconductivity of the PAT6/TiO_2 composite increased markedly and is discussed, taking the photoinduced charge transfer between PAT6 and TiO_2 into consideration (see Fig. 1).

2. Experimental

2.1 *Materials*

TiO_2 powder (P25) was donated by Degussa AG, Frankfurt, in the form of 30% rutile and 70% anatase, with an average particle size of approximately 21 nm. 3-Hexylthiophene was purchased from Aldrich. All other solvents and chemicals were of analytical reagent grade and were obtained from Nacalai Tesque, Japan.

2.2 *Synthesis of PAT6/TiO_2 nanocomposites*

The PAT6/TiO_2 composites were prepared by the chemical oxidation of hexylthiophene with $FeCl_3$ in the presence of dispersed TiO_2. The 3-hexylthiophene–TiO_2 complex was prepared by mixing 3-hexylthiophene and TiO_2 at a stoichiometric ratio in chloroform with ultrasonic dispersion for 2 h at 0°C, until a dispersive 3-hexylthiophene–TiO_2 complex was obtained. Polymerization was carried by slowly adding a slurry of $FeCl_3$ in chloroform into above-mentioned 3-hexylthiophene–TiO_2 complex solution over a period of 4 h at 0°C followed by ultrasonic dispersion of the mixture for another 2 h. The final concentration proportion of the monomer to $FeCl_3$ was maintained to be 1 : 4. The treatment of the reaction mixture with methanol resulted in the precipitation of PAT6/TiO_2, which was carefully dedoped by repeatedly treating a chloroform solution of PAT6/TiO_2 with concentrated ammonia. The chloroform solution was then filtered, concentrated to a small volume and PAT6/TiO_2 was precipitated from methanol and collected by membrane filtration.

2.3 *Fabrication of photovoltaic device*

The chloroform solution of PAT6/TiO_2 was spin-coated onto ITO glass. The Al electrode was fabricated by thermal evaporation through a shadow mask onto the PAT6/TiO_2 layer under a pressure of 10^{-4} Pa as a counterelectrode to the ITO electrode. The typical electrode area of photovoltaic cell was $1 \times 1\ mm^2$. In this cell, the ITO and Al electrodes play roles as electron and hole collector, respectively.

2.4 *Characterization*

The measurements of particle sizes of PAT6/TiO_2 composites and observations of the nature of association between TiO_2 and PAT6 were performed using a Hitachi 8000 transmission electron microscope and a Hitachi S-2100A scanning electron microscope, respectively. The FTIR measurement of the composite was carried out on a JASCO Corporation FT/IR-300E. X-ray diffraction measurements using Cu Kα radiation were performed by powder XRD (RINT 1100, Rigaku). Absorption was measured using a Hitachi 330 UV–vis spectrophotometer. Photoelectrical measurements were carried out in a vacuum optical cryostat at about 10^{-5} Torr. The current–voltage characteristics were measured with a Keithley 237 high-voltage source measurement unit in the dark and under illumination with monochromatic light. A high-intensity xenon lamp (500 W) was used as UV–vis light source. The spectral response of the device was corrected for the response of the lamp-monochromator system by measuring the calibration spectrum with UV-enhanced Si photodiode placed in the sample position.

3. Results and Discussion

In order to determine the particle sizes of PAT6/TiO_2 composites and to observe the nature of association between the PAT6 and TiO_2, samples were studied by SEM and TEM, respectively, which are summarized in Figs. 2 and 3. Figures 2(a) and 2(b) are the typical SEM images of PAT6/TiO_2 composites with TiO_2 weight fractions of 25 and 50%, respectively. Figure 2(a) shows the particles of nanocomposite materials prepared using the ultrasonic-assisted synthesis method, which shows clearly that the diameters of PAT6/TiO_2 composite in size range from 30 to 50 nm and that several particles are about 100 nm because of the aggregation of TiO_2 particles. The SEM images also clearly show that in the PAT6/TiO_2 composite a large number of globules are aggregated. However, as TiO_2 weight fractions increases, the particle diameter decreases, which leads to the changes in the surface morphological structure of aggregated composites from a loose cotton like to a firm gravel-like appearance as shown in Fig. 2(b). Furthermore, the PAT6/TiO_2 nanocomposites with a TiO_2 content of 50% were similar to those of 25% and more homogeneous than those of 25% [Fig. 2(b)].

In Fig. 3(a), the TEM image of PAT6/TiO_2 nanocomposites with a TiO_2 weight fraction of 50% shows uniformly dispersed particles of approximately 30–40 nm size, which are larger than TiO_2 particles. Concerning TiO_2 particles, there are polydisperse spheres of approximately 20 nm. After composite formation, these particles were found to be entrapped in the PAT6 chain leading to the increase in particle size. Therefore, the TiO_2 particles do not simply mix or blend with PAT6, but they are rather bound to the PAT6 chains. The polymer layer on the surface of TiO_2 particles can be distinctly observed in Fig. 3(b) and the thickness of the polymer layer was lower than 10 nm. The PAT6/TiO_2

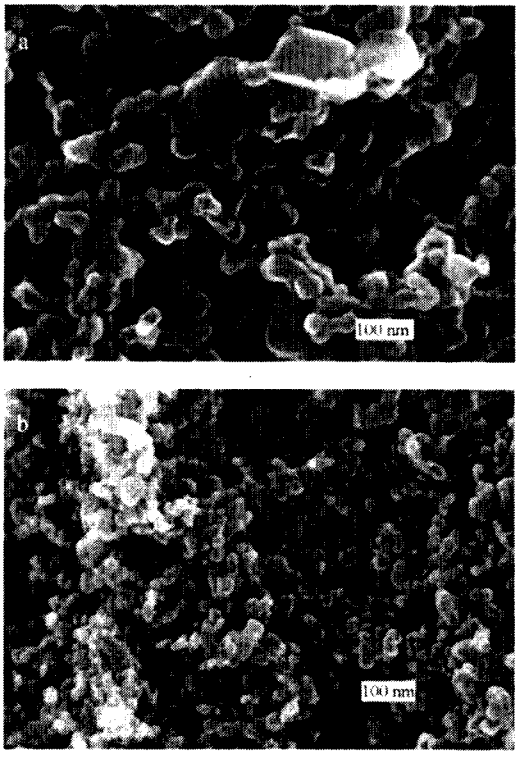

Fig. 2. SEM images of PAT6/TiO_2 with TiO_2 weight fractions of 25% (a) and 50% (b).

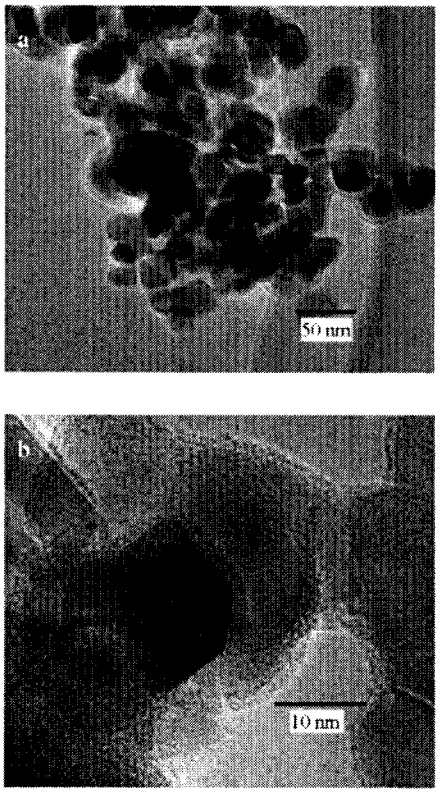

Fig. 3. TEM images of PAT6/TiO_2 (50%) (a) and PAT6/TiO_2 single particle (b).

composite is composed of polycrystalline parts and amorphous parts. The polycrystalline parts are distributed in the central field of the PAT6/TiO_2 nanocomposite and the amorphous parts are distributed in the field far from the central field of the PAT6/TiO_2 nanocomposite, which is due to the restrictive effect of the surface of TiO_2 while PAT6 chains grow.

The FTIR spectra of PAT6, PAT6/TiO_2 (25%) and PAT6/TiO_2 (50%) are shown in Figs. 4(a)–4(c), respectively. As shown in Fig. 4(a), there are characteristic bands at 2925 and 2858 cm^{-1}, which correspond, respectively, to the asymmetric C–H stretching vibrations in $-CH_3$ and $-CH_2-$, and the symmetric C–H stretching vibration in $-CH_2-$.[20] They are ascribed to the hexyl side chain. The bands at 3057 and 828 cm^{-1} correspond to the stretching vibration of CH in the aromatic =C–H and the =C–H out-of-phase deformation of aromatic =C–H, and the C=C stretching band at 1450 and 1510 cm^{-1}, respectively. As noted in the FTIR spectrum for PAT/TiO_2 [Figs. 4(b) and 4(c)], the C=C band shifted to 1516–1454 cm^{-1} because of the increase in the conjugation length of the polymer. The bands near 1633 and 500 cm^{-1} correspond to the Ti–O stretching vibration of the Ti–OH group.[21,22] Moreover, the intensities of some peaks at 2925, 2858, 1510, 1450, and 825 cm^{-1} turned became weak while the intensities of the peak at 1633 cm^{-1} turned became strong and sharp as the TiO_2 content increased because of the effect of the presence of TiO_2 during PAT6 synthesis. Upon the introduction of TiO_2 particles into the reaction system, thiophene becomes adsorbed on the oxide particles during ultrasonic dispersion. Polymerization proceeds initially on the surface of these oxide particles when $FeCl_3$ is added to the reaction system. This leads to the

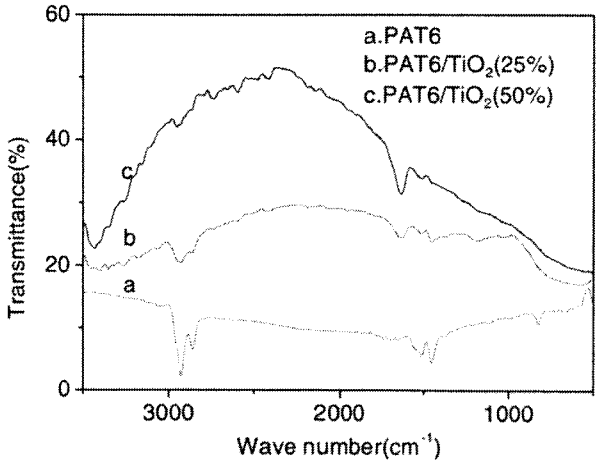

Fig. 4. FTIR spectra of PAT6 (a), PAT6 with TiO_2 weight fractions of 25% (b) and 50% (c).

adhesion of the polymer to the TiO_2 particles resulting in a constrained growth around the particles. Such adsorption and constrained motion of the chains will restrict the mode of vibration in PAT6, which will lead to the differences in IR spectra.

Figure 5 shows the XRD pattern of the prepared nanocomposite powders with different TiO_2 weight fractions. Curves 1, 2, 3 and 4 correspond to PAT6, PAT6/TiO_2 (25%), PAT6/TiO_2 (50%) and TiO_2, respectively. A study of the XRD patterns of the present samples revealed that PAT6 is an amorphous polymer as shown by curve 1 in

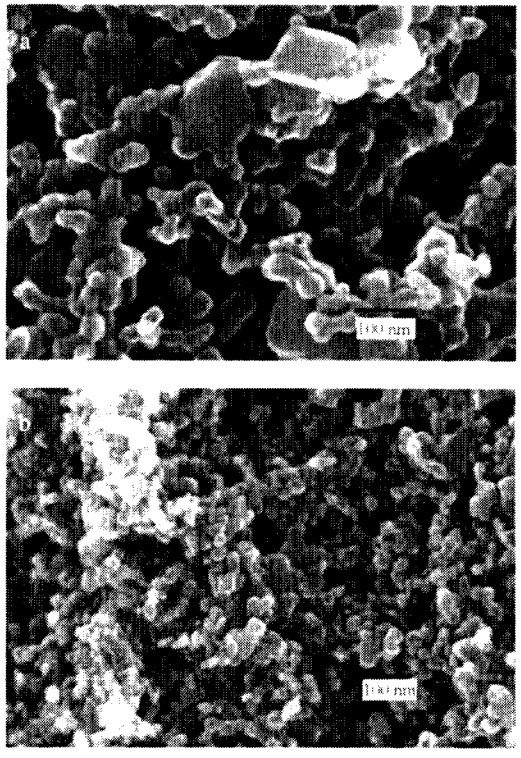

Fig. 2. SEM images of PAT6/TiO_2 with TiO_2 weight fractions of 25% (a) and 50% (b).

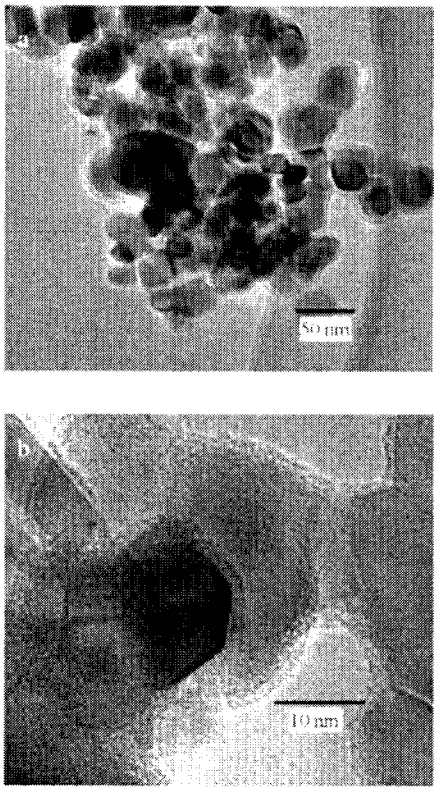

Fig. 3. TEM images of PAT6/TiO_2 (50%) (a) and PAT6/TiO_2 single particle (b).

composite is composed of polycrystalline parts and amorphous parts. The polycrystalline parts are distributed in the central field of the PAT6/TiO_2 nanocomposite and the amorphous parts are distributed in the field far from the central field of the PAT6/TiO_2 nanocomposite, which is due to the restrictive effect of the surface of TiO_2 while PAT6 chains grow.

The FTIR spectra of PAT6, PAT6/TiO_2 (25%) and PAT6/TiO_2 (50%) are shown in Figs. 4(a)–4(c), respectively. As shown in Fig. 4(a), there are characteristic bands at 2925 and 2858 cm^{-1}, which correspond, respectively, to the asymmetric C–H stretching vibrations in $-CH_3$ and $-CH_2-$, and the symmetric C–H stretching vibration in $-CH_2-$.[20] They are ascribed to the hexyl side chain. The bands at 3057 and 828 cm^{-1} correspond to the stretching vibration of CH in the aromatic =C–H and the =C–H out-of-phase deformation of aromatic =C–H, and the C=C stretching band at 1450 and 1510 cm^{-1}, respectively. As noted in the FTIR spectrum for PAT/TiO_2 [Figs. 4(b) and 4(c)], the C=C band shifted to 1516–1454 cm^{-1} because of the increase in the conjugation length of the polymer. The bands near 1633 and 500 cm^{-1} correspond to the Ti–O stretching vibration of the Ti–OH group.[21,22] Moreover, the intensities of some peaks at 2925, 2858, 1510, 1450, and 825 cm^{-1} turned became weak while the intensities of the peak at 1633 cm^{-1} turned became strong and sharp as the TiO_2 content increased because of the effect of the presence of TiO_2 during PAT6 synthesis. Upon the introduction of TiO_2 particles into the reaction system, thiophene becomes adsorbed on the oxide particles during ultrasonic dispersion. Polymerization proceeds initially on the surface of these oxide particles when $FeCl_3$ is added to the reaction system. This leads to the

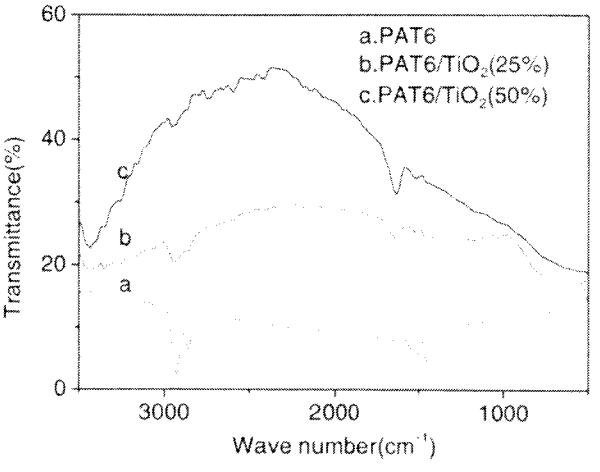

Fig. 4. FTIR spectra of PAT6 (a), PAT6 with TiO_2 weight fractions of 25% (b) and 50% (c).

adhesion of the polymer to the TiO_2 particles resulting in a constrained growth around the particles. Such adsorption and constrained motion of the chains will restrict the mode of vibration in PAT6, which will lead to the differences in IR spectra.

Figure 5 shows the XRD pattern of the prepared nanocomposite powders with different TiO_2 weight fractions. Curves 1, 2, 3 and 4 correspond to PAT6, PAT6/TiO_2 (25%), PAT6/TiO_2 (50%) and TiO_2, respectively. A study of the XRD patterns of the present samples revealed that PAT6 is an amorphous polymer as shown by curve 1 in

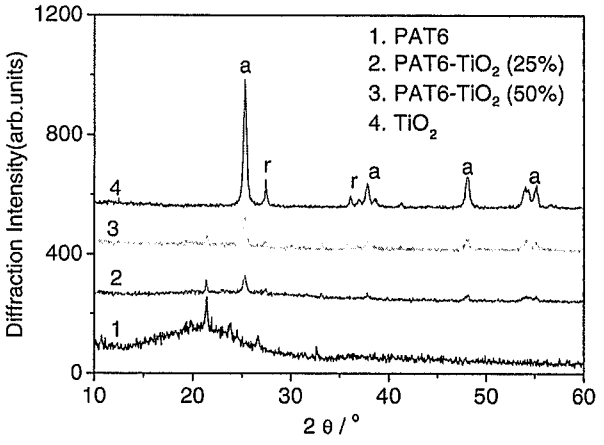

Fig. 5. XRD patterns of PAT6 (1), PAT6 with TiO_2 weight fractions of 25% (2) and 50% (3), respectively, and TiO_2 (4).

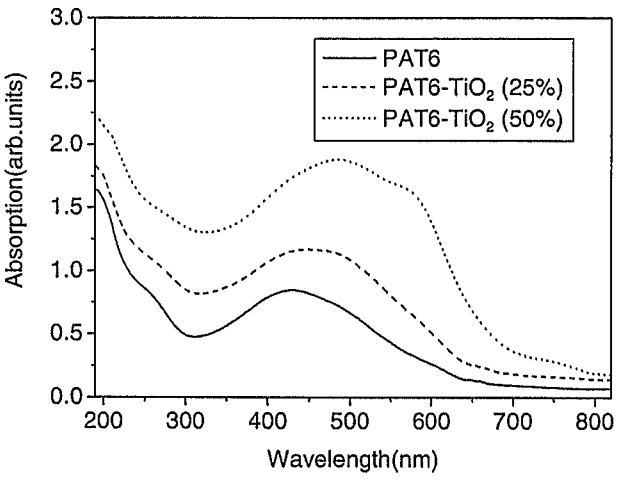

Fig. 6. UV–vis absorption spectra for PAT6 and PAT6 with TiO_2 weight fractions of 25% and 50%.

Fig. 5. For the composites of PAT6/TiO_2 with different TiO_2 contents, identical XRD patterns are observed as curves 2 and 3 in Fig. 5. When the PAT6 chains were stacked around TiO_2 particles, the broad weak diffraction peaks of PAT6 disappeared evidently, while new strong sharp diffraction peaks evolved at $2\theta = 21.4$, 23.8, 25.3, 26.5, 27.4, 36.1, and 37.8° with increasing TiO_2 content in the composite. The peaks of $2\theta = 25.3$, 27.4, 36.1, and 37.8° correspond to the diffraction of TiO_2 particles. The peaks at $2\theta = 25.3$, 37.8, 48.1, and 54.2° can be ascribed to the anatase phase and the peaks at $2\theta = 27.4$ and 36.1° to the rutile phase.[23] New peaks appeared at $2\theta = 21.4$ and 33.2°, which indicates the existence of interactions between PAT6 and TiO_2. The components of these new phases are not well known at the moment. We considered that the new diffraction may originate from the PAT6 chain, which indicates that a structure with a poor crystallinity was formed during the polymerization with a constrained growth around TiO_2 particles. During polymerization, the growth of the PAT6 chain is considered to be restricted around TiO_2 particles and the PAT6 chain around TiO_2 particles is in a crystalline state. With the increase in TiO_2 content in composites, these peaks become sharper and the size of the amorphous scattering region decreases. This implies that the composite samples have a more ordered arrangement than the PAT6 chain, which is also reflected in their TEM images.

The UV–vis absorption spectra of films of PAT6 and PAT6/TiO_2 with TiO_2 weight fractions of 25 and 50% are depicted in Fig. 6. The PAT6 film exhibited the onset absorption at 639 nm while the PAT6/TiO_2 films with TiO_2 weight fractions of 25 and 50% exhibited onset absorption at 673 and 708 nm, respectively. Compared with the PAT6 film, peak intensity increased and peak width increased in the PAT6/TiO_2 film. As the TiO_2 content increased, the spectra of PAT6/TiO_2 nanocomposites red-shifted compared with PAT6, which indicated the conjugation length of the PAT6/TiO_2 nanocomposite is large than that of PAT6 in the case of TiO_2 as the polymerized core.[24] The spectra of nanocomposites showed a sharp absorption edge and a well-defined shoulder on the edge, which generally contributed to an increase in the chain order. These phenomena suggest that the increase in effective surface area between the polymer

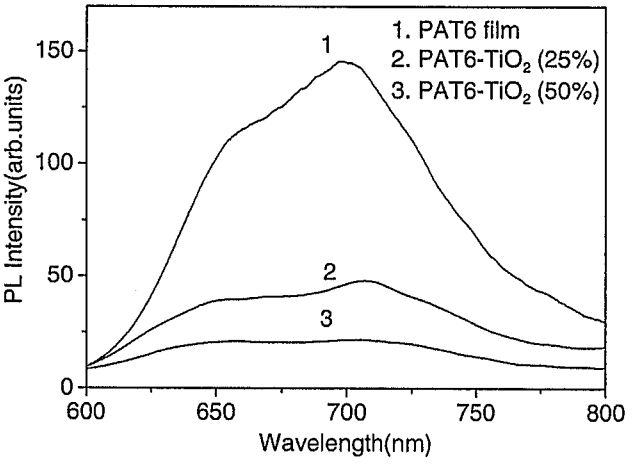

Fig. 7. Photoluminescence spectra for PAT6 (1) and PAT6 with TiO_2 weight fractions of 25% (2) and 50% (3).

and TiO_2 leads to a more efficient absorption and hence, a better performance in terms of photocurrent.

The photolumincence (PL) spectra of films of PAT6 and PAT6/TiO_2 with TiO_2 weight fractions of 25 and 50% are shown in Fig. 7. As is evident, the PL intensity of the PAT6/TiO_2 film at 697 nm is significantly quenched compared with that of the PAT6 film as TiO_2 content increased. If we regard the pristine PAT6 film PL intensity as 1, the PL intensities of the films of PAT6/TiO_2 with TiO_2 weight fractions of 25 and 50% decrease to 0.32 and 0.14, respectively. It should be noted that upon the covering of TiO_2 with the PAT6 layer, the PL intensity peak of PAT6/TiO_2 films with TiO_2 weight fractions of 25 and 50% red-shifted to 710 nm as compared with PAT6. These phenomena were identical to the results of absorption and indicated that the chain order and π-electron delocalization increased with the increase in TiO_2 weight fraction. This suggests that electron transfer from PAT6 to TiO_2 does occur and that the charge transfer is sufficiently rapid to compete with the radiative recombination of excitons in PAT6.

The photovoltaic effects in films of PAT6 and PAT6/TiO_2

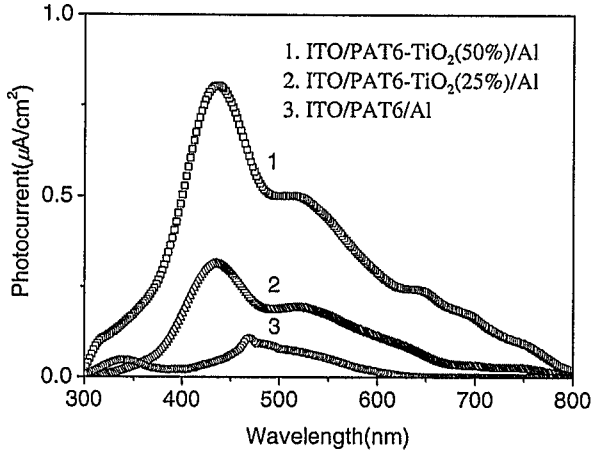

Fig. 8. Photocurrent spectra of PAT6 (3) and PAT6 with TiO_2 weight fractions of 25% (2) and 50% (1).

with TiO_2 weight fractions of 25 and 50% were studied by fabricating single-layer devices, ITO/PAT6/Al, ITO/PAT6/TiO_2 (25%)/Al and ITO/PAT6/TiO_2 (50%)/Al. Figure 8 shows the photocurrent spectra of the devices under illumination by a 500 W xenon lamp. A comparison of results shows that the device fabricated using the PAT6/TiO_2 film exhibits a better performance with regards to photocurrent than that fabricated using the PAT6 film throughout nearly the entire visible wavelength range. The difference in photoresponse between the PAT6 and PAT6/TiO_2 cells can be explained as follows. In PAT6/TiO_2 photovoltaic devices, efficient exciton dissociation is known to occur at the donor/acceptor (PAT6/TiO_2) heterojunction due to a small diffusion length of Frenkel excitons in these materials, of the order of 20 nm,[25] and excitons, which are generated away from the D/A interface, fail to dissociate. This means that the charge separation of excitons occurs only at the PAT6 and TiO_2 interface between in the single-layer devices. The cells fabricated using the PAT/TiO_2 (50%) samples showed the highest photocurrent among all the samples, which were related to the large interfacial area and the low number of defects in the pore and aggregates, as shown in SEM and TEM images. The PAT6/TiO_2 (25%) film shows a large number of defects in the pore and aggregates. The effective sensitized area is small in the PAT6/TiO_2 (25%) interface, which generates a lower current density than in the PAT6/TiO_2 (50%) interface. The cells fabricated using the PAT6 samples showed the lowest photocurrent owing to their smallest interfacial area without TiO_2. In addition, the photocurrent spectrum of the PAT6/TiO_2 devices exhibits a stronger response to the entire visible light range; some evident improvements were achieved in the wavelength range of 600–800 nm. These phenomena suggest that morphological differences attributed to TiO_2 play the most important role in conversion efficiency. Therefore, by controlling morphology, presently, researches aim to achieve bicontinuous percolating paths so that most of the excitons dissociate and the photogenerated carriers can be transported to the respective electrodes.

The photovoltaic characteristics of the three devices under illumination are listed in Table I. Both devices are irradiated with light at 500 nm and 45 $\mu W/cm^2$ in intensity from the ITO electrode side. The fill factor (FF) is defined as $FF = I_{max}V_{max}/I_{sc}V_{oc}$. Conversion efficiency (η) is defined as $\eta = I_{sc} \times V_{oc} \times FF/P_{opt}(\lambda)$, where I_{max}, $V_{max}I_{sc}$, V_{oc} and $P_{opt}(\lambda)$ are the current and voltage values for the maximum power in the I–V curve under illumination, the short circuit, the open circuit voltage and the incident light flux in $W\,cm^{-2}$, respectively. Comparing the conversion efficiencies between the ITO/PAT6/Al and the ITO/PAT6–TiO_2/Al devices, we observed that the conversion efficiency in the ITO/PAT6–TiO_2/Al devices increased to more than twofold that of ITO/PAT6/Al, owing to the increase in effective interface area. The experimental results show that the ITO/PAT6–TiO_2 (50%)/Al device exhibits a higher open-circuit voltage and a higher short-circuit current than the ITO/PAT6–TiO_2 (25%)/Al device and the ITO/PAT6/Al device under irradiation with monochromatic light at 500 nm. The higher open-circuit voltage and the higher short-circuit current can possibly be attributed to an efficient charge separation by successive electron transfers from PAT6 to TiO_2 in the active layer.

Table I. Photovoltaic characteristics of devices under illumination.

Structure of device	I_{sc} ($\mu A/cm^2$)	V_{oc} (mV)	FF (%)	η (%)
ITO/PAT6/Al	0.058	92	18	0.002
ITO/PAT6–TiO_2(25%)/Al	0.173	165	22	0.014
ITO/PAT6–TiO_2(50%)/Al	0.392	196	25	0.043

4. Summary

PAT6/TiO_2 nanocomposites with different TiO_2 weight fractions were synthesized by in situ ultrasonic-assisted polymerization. TiO_2 particles were encapsulated in the cores of the growing polymer chains, resulting in the formation of an inorganic-organic nanocomposite material. The interaction between PAT6 and TiO_2 and the nature of chain growth were investigated and explained according to the results of FTIR. The increase in conjugation length of the polymer and the improvement of crystallinity with an increase in TiO_2 weight fraction were investigated and explained according to the results of UV–vis absorption spectroscopy, photoluminescence spectroscopy and XRD. Particle dimensions were measured and the nature of association between the components was observed by SEM and TEM techniques. The improvement of photoconductivity was discussed in terms of the photoinduced charge transfer. The improvements in various physical properties of the present nanocomposite are expected to enhance the application potential of the conducting polymer without adversely affecting its chemical properties.

Acknowledgment

This work was supported by the National Natural Science Foundation of China (No. 60307001) and the Natural Science Foundation of Tianjin City (No. 05YFJMJC08800).

1) A. Fujii, A. Zakhidov, V. Borovkov, Y. Ohmori and K. Yoshino: Jpn. J. Appl. Phys. **35** (1996) L1438.
2) K. Tada, M. Onoda, H. Nakayama and K. Yoshino: Synth. Met. **102** (1999) 982.
3) M. G. Harrison and J. Gruner: Synth. Met. **84** (1997) 653.

4) S. Morita, A. A. Zakhidov and K. Yoshino: Solid State Commun. **82** (1992) 249.
5) K. Yoshino, X. H. Yin, S. Morita, T. Kawai and A. A. Zakhidov: Chem. Express **7** (1992) 817.
6) K. Yoshino, X. H. Yin, S. Morita, T. Kawai and A. A. Zakhidov: Solid State Commun. **85** (1993) 85.
7) M. A. Hamon, J. Chen, H. Hu, Y. S. Chen, M. E. Itkis, A. M. Rao, P. C. Eklund and R. C. Haddon: Adv. Mater. **11** (1999) 834.
8) W. Feng, X. D. Bai, Y. Q. Lian, X. G. Wang and K. Yoshino: Carbon **41** (2003) 1551.
9) D. Y. Godovsky: Adv. Polym. Sci. **153** (2000) 163.
10) R. Plass, S. Pelet, J. Krueger, M. Gratzel and U. Bach: J. Phys. Chem. B **106** (2002) 7578.
11) E. Kymakis, I. Alexandrou and G. A. J. Amaratunga: J. Appl. Phys. **93** (2003) 1764.
12) W. U. Huynh, J. A. Dittmer and A. P. Alivisatos: Science **295** (2002) 2425.
13) A. J. Breeze, Z. Schlesinger, S. A. Carter and P. J. Brock: Phys. Rev. B **64** (2001) 125205.
14) C. Y. Kwong, W. C. H. Choy, A. B. D. Jurisic, P. C. Chui, K. W. Cheng and W. K. Chan: Nanotechnology **15** (2004) 1156.
15) L. B. Roberson, M. A. Poggi, J. Kowalik, G. P. Smestad, L. A. Bottomley and L. M. Tolbert: Coord. Chem. Rev. **248** (2004) 1491.
16) M. Gratzel: Prog. Photovolt. Res. Apl. **8** (2000) 171.
17) B. Zhenan, A. Dodabalapur and A. J. Lovinger: Appl. Phys. Lett. **69** (1996) 4108.
18) H. Sirringhaus, N. Tessler and R. H. Friend: Science **280** (1998) 1741.
19) W. Feng, T. Umeda, A. Fujii, X. G. Wang and K. Yoshino: Jpn. J. Appl. Phys. **43** (2003) 3473.
20) E. W. Tasai, S. Basak, J. P. Ruiz, J. R. Reynolds and K. Rajeshaw: J. Electrochem. Soc. **136** (1989) 3683.
21) J. Zhang, B. Wang, X. Ju, T. Liu and T. Hu: Polymer **42** (2001) 3697.
22) B. D. Yang and K. H. Yoon: Synth. Met. **142** (2004) 21.
23) B. R. Sankapal, M. C. L. Steiner and A. Ennaoui: Appl. Surf. Sci. **239** (2005) 165–170.
24) T. W. Hagler, K. Pakbaz, K. F. Voss and A. J. Heeger: Phys. Rev. B **44** (1991) 8652.
25) N. C. Greenham, X. Peng and A. P. Alivisatos: Phys. Rev. B **54** (1996) 17628.